Grain size variability in debris flows of different runout lengths, Wenchuan, China

Erin L. Harvey[1,2,*], Tristram C. Hales[1], Jie Liu[3], Daniel E. J. Hobley[1,4], Fan Yang[3], Bing Xia[3], Xuanmei Fan[3]

[1] School of Earth and Environmental Science, Cardiff University, Cardiff UK.

[2] Now at: Department of Geography, Durham University, Durham, UK

[3] State Key Laboratory for Geohazard Prevention and Geoenvironment Protection, Chengdu University of Technology, Chengdu, China

[4] RSK ADAS Ltd, Helsby, Cheshire, UK

** Corresponding author (Erin.L.Harvey@durham.ac.uk)*

ABSTRACT

Debris flow grain size distributions (GSD) control runout length and mobility. Wide, bimodal GSDs and those containing a higher proportion of silt and clay have been shown experimentally to increase runout length. However, the relationship between grain size and mobility has not been well established in field conditions. Here we compare the grain size characteristics of two debris flows with considerably different runout lengths (1.5 km vs. 8 km) to understand the role of grain size in governing runout. The two debris flows were triggered in same rainfall event from co-seismic landslide debris generated in the 2008 Wenchuan earthquake in catchments with similar lithology and topography. We compare the deposited GSDs and their spatial pattern using our rare, three-dimensional GSD datasets. Surprisingly, the proportions of each size fraction deposited by the two flows were statistically indistinguishable. The spatial pattern of grain size differed between the two flows, with evidence of inverse grading only preserved in the smaller deposit. From these observations, we can infer that the GSDs of both flows were determined by the co-seismic

landslide source material, and that there was little difference in the GSD of material entrained as the flows bulked. The contrasting spatial distribution of grains indicates that different internal processes were dominant within the two flows. These findings demonstrate that where GSDs are dominated by coarse grains and governed by similar source conditions, grain size plays a lesser role relative to sediment supply and hydrology in controlling the runout length of large catastrophic post-earthquake debris flows.

INTRODUCTION

Debris flows rapidly travel across long distances at relatively shallow gradients in comparison to other landslide types, posing a major hazard to many communities (Takahashi, 2007). The mobile nature of debris flows can be attributed to their higher water content and the wide range of grain sizes that they transport. Debris flows are one of few processes on Earth able to transport clay to boulder sized material (>10 m) (Iverson, 1997). The relative proportions of each grain size can be used to infer rates of sediment export by fluvial processes (Sklar et al., 2017, 2020), the potential for debris flow reoccurrence (Domènech et al., 2019) as well as the runout length of debris flows (Iverson et al., 2010; de Haas et al., 2015). Controls on debris flow runout length have been explored in the field in relation to topography (e.g. channel slope and tributary junction angles) (Benda and Cundy, 1990). However few field studies have considered the relationship between grain size and runout length (Whipple and Dunne, 1992). Small- and large-scale flume experiments have demonstrated how GSDs can affect the hydrological and frictional properties of a debris flow (Iverson et al., 2010; de Haas et al., 2015; Kaitna et al., 2016). For example, the presence of fine sediment in wide GSDs can reduce the rate at which excess pore pressures dissipate within the flow and lead to longer runout lengths (Pierson, 1981; Major, 1997; Iverson et al., 2010; de Haas et al., 2015). In contrast, extremely high clay (e.g. 22% volume percent in small-scale flume experiments; de Haas et al., 2015) and gravel (e.g. 49% volume percent in

small-scale flume experiments; de Haas et al., 2015) contents can reduce the mobility and thus runout length of a debris flow by increasing the role of viscous and frictional forces respectively. An understanding of these relationships in a field context will be invaluable when using these experiments and model outcomes to better predict debris flow occurrence and runout length.

Debris flows often leave distinct deposits behind, consisting of snouts and levees, which are thought to reflect the mechanisms driving transport and deposition within the flow, such as segregation and particle collisions (Pierson, 1981; Whipple and Dunne, 1992; Blair and McPherson, 1998; Kim and Lowe, 2004). Kinetic sieving and squeeze expulsion can segregate grains by size, with the finer grains percolating between larger grains as the mixture jostles during transit, leading to the formation of inversely graded deposits, coarse debris flow levees and snouts (Johnson et al., 2012; Jones et al., 2023). Size segregation within debris flows can relate to debris flow properties. For example, debris flows with dominant frictional forces and high solid contents were more likely to produce a deposit with coarse levees and inverse grading, whereas segregation was often inhibited in highly viscous flows or flows with a high-water content where grain contacts were buffered by the fluid phase (Sohn et al., 1999; Vallance and Savage, 2000; Sosio et al., 2007). As debris flows traverse down catchments entraining material over variable topography, the GSD mobilized is likely to change also (Morell et al., 2021). The pattern of grains by size spatially within deposits may provide insight into debris flow properties and longitudinal change that relate to changes in source and in-channel material.

Flume experiments have explored the spatial evolution of grain size with distance downstream (Johnson et al., 2012; de Haas et al., 2015), however only a few studies have explored the changes in grain size with distance downstream for natural debris flow deposits (Vallance and Scott, 1997; Blair and McPherson, 1998; Kim and Lowe, 2004; Santi et al.,

2008). Field based assessments of debris flow grain size are challenging to obtain due to the heterogenous nature of deposits, the wide range of grain sizes that are difficult to accurately measure (from clay to boulders >10 m), and the inaccessible nature of deposits in mountainous locations (Vallance and Scott, 1997; Genevois et al., 2000; Chen et al., 2001; Harvey et al., 2022). Hence there has been a focus on flume experiments and numerical modelling to better understand debris flow GSDs and their relation to debris flow mobility (Bagnold, 1954; Major and Pierson, 1992; Takahashi et al., 1992; Major and Iverson, 1999; de Haas et al., 2015; Sanvitale and Bowman, 2017; Barker et al., 2021). There have been few attempts to compare the results of these experiments with field datasets to establish how the processes modelled may affect the runout of debris flows in nature. The collection of high-quality field datasets is essential to verify these experiments and numerical models and subsequently better understand the hazard posed by debris flows.

In this study, we seek to test the hypothesis that debris flow runout is controlled by changes in grain size. Specifically, we study two debris flows triggered in very similar source geologies to explore whether changes in grain size along the flow path control debris flow runout length. We collected a unique set of grain size measurements from two post-earthquake debris flows with different runout lengths. The debris flows initiated in August 2019 in the epicentral area of the 2008 M_w7.9 Wenchuan Earthquake (Figure 1). The Liusha debris flow had a modest runout of 1.5 km when compared to the 8 km runout of the Luoquan debris flow (Figure 2). We measured the GSDs for both debris flow deposits across three dimensions (vertically, laterally across cross sections of the deposit, and longitudinally with distance downstream) to collect high resolution spatial records (Figure 3). We also analysed the spatial pattern of deposition with respect to grain size to provide insight into the dominant internal processes within the two flows. We hypothesise that the two debris flows will be characterized by different GSDs, with the more mobile debris flow likely to have a

higher proportion of fine sediment, based on our understanding of the relationship between debris flow grain size and mobility outlined above.

METHODS

Sample locations

The Luoquan and Liusha debris flows were triggered by a period of intense rainfall on 20th August 2019 in the epicentral area of the 2008 M_w 7.9 Wenchuan Earthquake (Table 1). These post-earthquake debris flows were equidistant from the fault line and remobilized earthquake-generated sediment in both cases incorporating co-seismic landslide debris and channel debris (Yang et al., 2021). The source area of both flows consisted of Mesoproterozoic granitoids, with the Liusha debris flow running out over Paleozoic greywacke and shale in the lower reaches (Figure 2; Ma, 2002). Debris flow deposits filled the channel, with soil, vegetation and co-seismic landslide deposits covering the banks either side of the channel. The debris flow deposits were sampled in November and December 2019, approximately three months after the debris flows occurred. Significant reworking of the deposits prior to this analysis is therefore unlikely. Fluvial reworking in this location is particularly unlikely with almost 90% of co-seismic landslide material remaining on hillslopes over a decade after the earthquake (Figure S1) (Francis et al., 2022). The toes of deposits were not sampled to avoid any potential reworking by the main river channels and when reestablishing access to roads overtopped by the flows.

The Luoquan debris flow covered an area an order of magnitude larger than the Liusha debris flow (>420 000 m^2 compared to 33 000 m^2) and travelled over 8 km in length in comparison to 1.5 km for the Liusha debris flow (Figure 2). The Luoquan debris flow was therefore considered a catastrophic debris flow, characterized by its long runout, large volume and the entrainment of sediment during transit (Major et al., 2007) as well as its impact on downstream infrastructure (Tang et al., 2012; Yang et al., 2021). Local observations of the

125 catastrophic Luoquan debris flow described the flow as being highly fluidized. This
126 description is consistent with recordings for other catastrophic debris flows triggered in the
127 same event. We sampled eight pits along the lower 4 km of the channel in Luoquan (Figure
128 2D; Table S1). In Liusha, we sampled the lower 800 m of the debris flow, which had an
129 average width and slope of 8 m and 23° respectively (Figure 2B; Table S1). Both debris
130 flows were channelized, with the Luoquan flow travelling along a 4^{th} order stream before
131 depositing and the Liusha debris flow down a 2^{nd} order stream respectively. The channel of
132 the Liusha deposit was much steeper, which could also contribute to the differences in the
133 observed runout length (Benda, 1990; Benda and Cundy, 1990; Hungr et al., 2008).
134 Nonetheless, the triggering of these debris flows in the same storm and with similar source
135 locations provided a unique opportunity to better understand how debris flow GSDs change
136 along the flow path in a field context and whether this relates to debris flow runout.
137 ***Geomorphic background***
138 We measured channel cross sections at each pit location using a laser range finder. We
139 calculated the downstream slope and curvature between sampling locations using the JAXA
140 30 m resolution digital elevation model (DEM) and taking the first and second derivatives of
141 elevation. We acknowledge that the resolution of this DEM is coarse, and therefore smoothed
142 these profiles using locally weighted scatterplot smoothing (LOWESS) and a span of 0.3
143 (Cleveland, 1979) (Figure 2).
144 The Liusha debris flow was characterized by a bedrock channel until ~700 m downstream of
145 the triggering location, after which the channel consisted of debris flow deposited sediment
146 (Figure S1). The deposit was sampled on a range of slopes between 17° and 29° (Figure 2).
147 Channel slope decreased with increased distance from the triggering location. Channel width
148 increased alongside this decrease in slope from 4 m (Pit 1) to 15.8 m (Pit 4). The channel had

149 a negative curvature, which was calculated as the second derivative of elevation. Negative
150 curvature means that the channel had a concave, divergent profile.
151 The Luoquan debris flow was triggered in a larger, shallower fourth order catchment. At
152 least, the lower 5500 m of the 8000 m debris flow channel was inundated with sediment.
153 Channel slope decreased with distance downstream along the 4000 m section sampled, with
154 the greatest decrease in slope between 5000 m and 7000 m downstream (Figure 2). Channel
155 width and curvature were more variable and did not appear to relate to the distance from the
156 source. The widest section of the channel sampled was found 5500 m downstream from the
157 triggering locations (61.2 m, Pit 4) and the average channel width based on the eight
158 sampling locations was 42 m (Figure 2). All sampling locations, besides Pit 1, in Luoquan
159 also had a negative curvature and were therefore concave. Pit 1 (4000 m from the triggering
160 location) had a curvature value close to 0, which represented a planar, uniform slope.

161 **Grain size distributions**

162 ***Sieving***

163 We sampled both debris flow deposits at equidistant intervals from the debris flow toe to the
164 upmost accessible location. In Luoquan, we sampled eight pits from 4000 m to 7500 m
165 downstream of the triggering location at 500 m intervals (Figures 2C and 2D). In Liusha, we
166 sampled four pits located 700 m to 1500 m downstream of the triggering location, at 200 –
167 300 m intervals (Figures 2A and 2B). Pits were numbered based on their distance from the
168 triggering location, with Pit 1 found at the most upstream location and the remaining pits
169 numbered downstream (Figure 2). We excavated pits measuring 1 m x 1 m x 0.5 m at 10 cm
170 increments and sieved sediment in the field into four size fractions using 4 cm, 2 cm and 1
171 cm sieves. For grains longer than 8 cm we separately measured all three axes and weighed
172 the grain individually. We retained 1 kg of the sediment <1 cm to wet sieve in the laboratory
173 using the following sieve sizes; 0.8 cm, 0.4 cm, 0.2 cm, 0.1 cm, 0.05 cm, 0.025 cm, 0.0125

cm and 0.0063 cm (Bunte and Abt, 2001; Attal and Lavé, 2006; Attal et al., 2015; Harvey et al., 2022) (Figure 3C). The sediment collected in the pan following sieving (<0.0063 cm) formed the silt and clay proportion of the GSD. We conducted manual end point tests for the samples to ensure all grains had passed through each sieve (Dufresne and Dunning, 2017). Each pit took 4-6 hours to sample, limiting the maximum pit depth to 50cm. The sediment in each pit weighed at least 1000 kg, which ensured that most pits met, or were close to, the minimum weight limit set out in Church et al., (1987).

We sampled grains which covered multiple layers from the lowest layer to avoid disturbing any layers during sampling. We therefore applied a correction to redistribute the effect of the largest grains which covered multiple layers and ensured that GSDs measured for each pit were not biased by the fact coarse grains were always measured at their deepest point. When applying the correction, we assumed that grains with an intermediate axis (b-axis) longer than 10 cm covered more than one layer (each layer was 10 cm deep). We reallocated the weight of each grain over 10 cm systematically as we did not know the exact proportion of the grain in each layer. For example, for a 25 cm grain recorded in layer 5 (40 – 50 cm), 10 cm and 40% of the weight of the grain was assumed to be in layer 5, the equivalent (10 cm and 40% of the weight of the grain) was reallocated to layer 4 and then the remaining weight of the grain (20% by weight, 5 cm) was added to layer 3. All three layers therefore contained a 25 cm grain, however the weight of the grain relative to the layer GSD was distributed across the three layers. The layers which included the largest grain sampled for each pit are shown in Figures 4 and 5. This correction was crucial because grains which covered multiple layers were initially only sampled in the lowest layer, and hence biased vertical GSDs affecting interpretations of inverse grading. Applying this correction removes this bias.

Photo analysis

We followed the protocol outlined in Kellerhals and Bray (1971), Attal and Lavé (2006) and Harvey et al. (2022) to obtain surface GSDs across both deposits using manual photo counts and pyDGS (Buscombe, 2013). Photos were taken using an iPhone 8 at equidistant intervals along transects (~1 m sections) perpendicular to the direction of flow at points where we collected sieved data (Figure 3B). The transects ran from the right and left edges of the deposit. We ensured the photos were parallel to the surface by using a 0.5 m x 0.5 m frame to calculate the resolution of the photo in mm per pixel.

Where the largest grains had a b-axis less than one third of the image width, we used the automated, texture-based grain size analysis tool pyDGS to measure the GSD of the photos and used manual photos counts for the other images (Buscombe, 2013). We ran pyDGS to obtain GSDs for over 200 photos with a shape parameter of 0, inferred using sieving GSDs, and varied the maxscale (the maximum grain size the algorithm searches for) and resolution depending on each photo (Harvey et al., 2022). The shape parameter is used to fit pyDGS GSDs to a reference GSD, typically collected using sieving or manual photo counts. The shape parameter applied here was determined based on pits 1 in Liusha and Luoquan, as discussed in further detail in Harvey et al. (2022). The minimum grain size detected by pyDGS is ~6 pixels in length. Based on our image resolutions (average 0.25 mm pi^{-1}), the minimum grain size detected using pyDGS is ~2 mm. For manual photo counts, we applied a grid to each image and measured the b-axis of grains that intersected the gridlines, excluding repeats that intersected multiple gridlines. The photos taken along the transects did not capture the largest grain size fraction (>1 m) as the photos taken were approximately 1 m x 1 m. To also study the spatial pattern of boulders in Luoquan, we manually measured the number and b-axis of grains larger than 1 m in diameter between 5000 m and 6750 m downstream using drone images taken in November 2019 (Figures 2C and 3D). Photos were only at a high enough resolution and quality to conduct the analysis over this section of the

channel and for this deposit. An advantage of using these 2D methods to acquire GSDs is the ability to survey larger areas, which is useful for large mass movement deposits, without disturbing the deposit (Bunte and Abt, 2001; Purinton and Bookhagen, 2021). The methods also require less field time and can be quicker once algorithms have been tuned. However, 2D techniques cannot characterize subsurface sections of the deposit, which are crucial for identifying processes such as kinetic sieving in mass movement deposits (Dunning, 2006; Harvey et al., 2022).

GSD integral

We quantified the shape of the GSDs by integrating underneath the normalized percent coarser than curve. This method is particularly useful for quantifying the relative coarseness of the deposit, with a larger GSD integral caused by a larger proportion by weight, and thus curve area, in the upper end of the distribution (Figure S2). The use of a GSD integral to determine the coarseness of the distributions was supported by the strong correlations between D_{50} and D_{84} with the GSD integral (Figure S3). We normalized grain size by the maximum grain size obtained using each method. We used a maximum value of 570 mm for sieving for both debris flows (5 mm for the fine GSD integrals in Table S2) so that the GSD integrals could be compared between the two flows. For the GSD integrals calculated from pyDGS and manual photo counts we used maximum grain sizes of 801 mm and 399 mm for Luoquan and Liusha respectively. As such, the photo generated GSD integrals could not be compared between the two debris flows directly. We chose to vary the maximum grain size in this instance as the larger maximum grain size from manual photo count GSDs in Luoquan would mean that changes in the GSD deposited in Liusha were overlooked. The GSD integrals could also not be compared across methods as they had been normalized by a different maximum grain size. The positive relationships, which were found for all

247 percentiles above D_{50}, suggest that the GSD integral provides a single metric which can be
248 deemed appropriate to represent at least the coarsest 50% of the GSDs measured.

249 **RESULTS**

250 The GSDs in Liusha and Luoquan ranged over four orders of magnitude, from clay to
251 boulders with GSD integrals from 0.15 to 0.35 and 0.09 to 0.23 respectively (Figures 4, 5, S4
252 and S5). The maximum sieved grain sizes were similar in both debris flows; 570 mm in
253 Liusha and 420 mm in Luoquan. The full GSDs deposited by the two debris flows were
254 statistically indistinguishable, with a chi-squared test comparing the average GSDs for both
255 flows unable to reject the null hypothesis where the p value < 0.05 (Table S3, $\chi 2 = 4.82$, d.f.
256 = 11, p-value > 0.05). The average GSDs were calculated by averaging the frequency by
257 weight within each grain size bin for all pits in each deposit. Both debris flows were coarse,
258 with up to 70% of the total weight of the pit comprised of boulders more than 80 mm in
259 length.

260 Overall, the proportion of fine grains (silt and clay) were relatively consistent, accounting for
261 very little of the total pit weight for both debris flows (up to 1.8% of the total weight in
262 Liusha and up to 1% of the total weight in Luoquan). The proportions of the total weight
263 occupied by grains <5 mm were also relatively consistent between the deposits, with on
264 average 18% of the total weight <5 mm in Luoquan and 14% in Liusha (Figures S4 and S5).
265 When analyzing the finest grain size fractions as a proportion of the total weight of grains <5
266 mm, the GSDs were also similar, with comparable GSD integrals for 11 of the 12 pits
267 sampled (average GSD integral: 0.35 in Luoquan, 0.39 in Liusha) (Figure 6 and Table S2).
268 Pit 8, where a large proportion by weight was in the coarser grain size fractions, only had a
269 fine GSD integral of 0.21 due to a high sand fraction by weight relative to gravel. When
270 analyzing the fine grain size fractions only, the Liusha deposit had a clay and silt content at

least double the relative content by weight in Luoquan, however as mentioned above the fraction of silt and clay was <2% of the total weight in both deposits (Figure 6).

Vertical GSDs

Vertical segregation by normal and inverse grading was evident in 75% of the pits sampled along the Liusha debris flow (Figures 4 and S4). The GSDs deposited were normally graded in the first sampling location, 700 m downstream from the triggering location (Figure 4). The deposit was then inversely graded in the two middle pits, which were located 1000 m and 1300 m downstream from the triggering location (Pits 2 and 3). The pit located furthest downstream (Pit 4) displayed no evidence of normal or inverse grading (Figure 4D). Normal and inverse grading can be observed using the GSDs for each layer as well as their GSD integrals (Figures 4 and S4).

There was no evidence for size segregation in the Luoquan debris flow (Figures 5 and S5). In sections of the deposit where a large grain covered all five layers, the GSD integrals varied the least (Figure 5). The layers with the largest grains were not always the coarsest layer in the pit (Figure 5). The GSDs deposited by the debris flow remained consistent in the pits located furthest upstream (4000 m to 6500 m downstream from the triggering location), with the proportion of sand, gravel and finer grains varying by up to 10% between layers (Figure S5). Across this 2500 m section of the deposit, the layer with the coarsest and finest GSD differed in each location.

Lateral (surface) GSDs

In both deposits, there was no consistent pattern in surface grain size with peaks in surface coarseness both at the edges and in the center of the deposits. No paired levees were evident in either debris flow (Figures 7 and 8). However, in the middle section of the Liusha debris flow deposit (1000 m to 1300 m downstream from the triggering location), the highest GSD integrals were found on the inner edge of the deposit around slight bends in the debris flow

296 channel (Figures 2A, 7C and 7E). This section of channel was also inversely graded (Figures
297 4B and 4C). Further downstream, coarse surface GSDs were found in both the center and on
298 the right side of the deposit (Figure 7G).
299 In Luoquan, the distribution of surface coarseness was not clearly linked to downstream
300 location, lateral position in the flow and channel cross section morphology (Figure 8).
301 Channel width appeared to be the main control on deposit coarseness (Figures 2 and 8). For
302 example, as channel width increased between Pits 1 and 3 (4000 m to 5000 m downstream of
303 the triggering location), there was also an increase in the relative coarseness of the deposit
304 surface, with higher GSD integrals 5000 m downstream where channel width increased to
305 43.5 m (Figure 8E). The largest variation in the surface grain size of the deposit were found
306 in Pits 3 (5000 m downstream) and 4 (5500 m downstream) corresponding to the dramatic
307 increase in channel width (Figures 2, 8E, and 8G).
308 **Longitudinal (surface and subsurface) GSDs**
309 In Liusha, there was a general decrease in the GSD integral with distance downstream for
310 both subsurface and surface GSDs (Figures 3D and 9). GSD integrals in Liusha fine abruptly
311 between 700 m and 1000 m downstream, which is likely related to the high proportion by
312 weight of sand and pebbles in the lower three pits and the strong relationship between GSD
313 integrals and the coarsest fraction (Figures 9C and 9D). There was a small increase in the
314 GSD integral between 1000 m and 1300 m downstream (Figure 9B). Channel width increases
315 gradually until 1300 m downstream, where there is a doubling in the channel width over a
316 200 m distance. At the point where width changes, the proportion of cobbles increases
317 (Figure 9D).
318 Longitudinal GSDs for Luoquan were sensitive to channel topography (Figure 10). Changes
319 in downstream curvature in the first five pits (Pits 1 to 5) corresponded to changes in the
320 fractions of fine sand, silt and clay deposited (Figure 10). More fine sand, silt and clay was

deposited when the decrease in channel slope downstream was sharper, and curvature was more negative (Figure 10). However, coarseness within the three pits located furthest downstream (Pits 6 to 8, between 6500 m and 7500 m downstream) did not correlate well with curvature. The maximum boulder size observed using drone imagery (3.7 m) corresponded to a decrease in channel width between Pits 6 and 7, 6750 m from the triggering location (Figures 10B and 10C).

DISCUSSION

Comparison of deposited GSDs

Both debris flows deposited a similar range of grain sizes (from clay to boulders) and similar relative proportions of these grains (Figure S6 and Table S3). These findings are inconsistent with the hypothesis that GSDs differ along the length of the flow to account for the observed differences in runout. Physical experiments have shown that flows with a higher proportion of clay and silt, and potentially wider GSDs, result in longer runouts. The presence of clays and silts within the pore spaces of the flowing matrix reduce the rate that excess pore pressures dissipate. Excess pore pressures generate liquefaction that increases the mobility of the flow. Hence slow excess pore pressure dissipation lead to flows that are mobile for longer and travel greater distances (de Haas et al., 2015). However, measurements of clays and silts did not vary significantly between the two flows, despite the differences in mobility (Figure 6 and Table S2). The clay and silt fraction accounted for less than 2% of the total grain size by weight, with the smaller Liusha flow depositing a higher proportion of clay relative to the total weight of all fine grains (<5 mm). The silt and clay content in the debris flows we measured was low relative to others measured in the field. For example, the Osceola mudflow had a clay content between 6% to 12% of the total weight and up to 25% of the total weight when combined with silt (Vallance and Scott, 1997). The low values for the debris flows in our study reflect the extremely coarse nature of the deposits and the abundance of

346 gravel sized grains and larger (Figures 6, S4 and S5). Samples from debris flows in Owens
347 Valley were also finer in comparison to the flows observed here, with 40% to 60% of
348 deposits comprised of sand (Whipple and Dunne, 1992). In our debris flows the proportion of
349 grains less than gravel (<2 mm) in size was below 33% at all locations. It is therefore
350 surprising that the Luoquan debris flow was able to travel across such long distances despite
351 a fine content far below that recorded for previous debris flows. We note however that fine
352 grains can be immediately removed from debris flow deposits as part of the interstitial fluid
353 phase and that the values for the proportion of clay and silt will have a degree of uncertainty,
354 as is the case with samples from all debris flow deposits (Shakesby and Matthews, 2002).
355 Based on the large volumes of both flows, it is unlikely that most fine sediment was removed
356 during transit. The small fraction of silt and clay in both flows, even when accounting for the
357 fact that there was double by weight the amount of clay and silt in Liusha, indicates that the
358 fine grain fraction is not the primary control on runout length for either of these flows.
359 If the GSDs do not significantly affect the runout length of the two flows, then we need an
360 alternative explanation for the observed runouts. The similar GSDs in both debris flows
361 reflect the consistent geology in the source regions as well as the fact both debris flows were
362 a combination of co-seismic landslide debris and channel sediment derived from eroded co-
363 seismic landslides. However, the volume of co-seismic landslide debris in both locations was
364 different, with the larger flow triggered in a catchment with a greater volume of debris. In this
365 case, the length of the different flows could reflect limitations in the volume of material that
366 could be entrained during the flow process (Yang et al., 2021) or the ability of the debris flow
367 to rapidly entrain material during transit, which can relate to the water content of the bed
368 material and flow (Figure 2) (Iverson et al., 2011).

369 **Spatial grain size patterns: segregation**

370 ***Vertical GSD trends***

Vertical grain size segregation occurred within the Liusha deposit, which was smaller and more topographically constrained, particularly along the steep middle reaches (24.7° and 21°). Two processes primarily control reverse grading: kinetic sieving, the percolation of smaller grains through gaps separating larger grains, and squeeze expulsion, a process by which all grains are levered upwards resulting in a net flux of smaller grains at the base (Vallance and Savage, 2000; Gray et al., 2015). These processes are commonly found when frictional forces and active particle collisions enable dilation and encourage segregation during the flow (Pierson and Costa, 1987; Kim et al., 1995; Vallance and Savage, 2000; de Haas et al., 2015). For example, reverse grading in the Rossiga debris flow, central Italian Alps occurred when high solid volume fractions produced more pronounced frictional and dispersive forces (Sosio et al., 2007). The small section of reverse graded deposits in Liusha supports the fact that both debris flows transported a large proportion of coarse grains. Evidence of grain size segregation in the Luoquan deposit is less clear, with finer surface and base layers in the pits further downstream, Pits 7 and 8 respectively, the only locations with clear changes in the grain sizes deposited by the flow (Figure S5). A lack of segregation may not be surprising for a very mobile flow with high pore fluid pressures that lubricate clast contacts and therefore reduce particle collisions in the flow (Sohn et al., 1999; Vallance and Savage, 2000). There are other mechanisms that could contribute to the lack of segregation such as incremental deposition (Vallance and Scott, 1997; Sohn et al., 1999), high turbulence within the flow which prevents mixing and segregation (Shultz, 1984) and high viscosity (Vallance and Savage, 2000). Observations by witnesses of the catastrophic debris flows in Luoquan and the surrounding catchments highlighted their highly fluidized and possibly turbulent nature (Guo et al., 2016; Yang et al., 2021). Where we did see segregation in the Liusha debris flow it occurred in areas where the channel width or slope changed. Segregation by grain size can also occur due to a decrease in velocity because of a decrease

396 in channel slope (Vallance and Savage, 2000). The velocities of both debris flows are not
397 known but the large difference in runout length and width of the Luoquan debris flow implies
398 a higher velocity irrespective of slope. Small changes in coarseness associated with
399 differences in channel slope demonstrate that topographic induced changes in flow velocity
400 could also play a minor role in the grain sizes deposited by the flows (Figures 9 and 10).

401 ***Lateral GSD trends***

402 Paired levees were not observed in our flows, however there were some levees preserved on
403 the inner banks of bends (Figures 7C and 7E). Paired levees are commonly found in
404 unconfined debris flows, such as those on open hillslopes and when debris flows escape
405 lateral confinement (Cannon et al., 2001; Iverson et al., 2010; Jones et al., 2023). Liusha and
406 Luoquan were confined by steep hillslopes on both sides, which may explain the absence of
407 levees. The absence of levees in Luoquan is consistent with the lack of vertical segregation
408 by grain size (Figure 5) (Johnson et al., 2012; Jones et al., 2023). Major (1997) also found
409 that levees were less likely to form in saturated flows, consistent with suggestions of high
410 pore fluid pressures in Luoquan.

411 Unpaired levees were found in sections of both debris flows (Figures 7C, 7E, 8G and 8K)
412 (Benda, 1990; Cenderelli and Kite, 1998). Coarsening at one edge of the channel may be
413 explained by variations in lateral flow velocity (Johnson and Rodine, 1984). In the middle
414 reaches of the Liusha deposit, the coarsest edges were found on the inner bend of the channel
415 (Figures 2 and 7). A levee deposit on the inner bend of the Luoquan deposit was observed in
416 the field 6500 m from the triggering location (see Pit 6 in Figures 2 and 8K). These levees on
417 the inner bend of the channel may relate to the anticipated lower flow velocities on the inner
418 bend because of centrifugal forces (Prochaska et al., 2008; Scheidl et al., 2015; Morell et al.,
419 2021). Prochaska et al. (2008) attributed inner bend levee formation to the upstream flow

momentum interacting with the channel wall or by sediment reflecting off the outer bend onto the inner bend in non-uniform bends, which could be possible for these debris flows.

Spatial grain size patterns: downstream evolution

Debris flow properties and GSDs did not change significantly with distance downstream. Relatively minor changes in GSD were evident with changes in topography (Figures 9 and 10). In Luoquan, the proportion of fines increased with decreases in curvature or steeper decreases in slope (Figures 10A, 10B and 10E). This observation may be related to a decrease in flow velocity and more rapid debris flow deposition once the debris flow stops, so more fine sediment is deposited (Takahashi, 1981; Cannon and Savage, 1988; Guthrie et al., 2010; Lanzoni et al., 2017). A decrease in the proportion of fine grains in the flow has the potential to create a feedback, whereby excess pore pressures in the flow may dissipate more rapidly and encourage further deposition (Pierson, 1981; de Haas et al., 2015). However, in the case of these flows there is no evidence of this mechanism occurring due to their highly fluidized nature. It is likely that the explanation for the enhanced fine content in deposits is more complex in this extremely large flow.

Channel width provided the strongest topographic control on GSDs in the Luoquan debris flow, as evidenced by the decreased deposition of boulders with increases in channel width and increased boulder frequency and size where the channel narrows (Figures 10B and 10C). At the widest reach sampled, we also found an increase in pebble content and a decrease in boulder frequency relative to the reach immediately upstream (Figures 8G and 10). The lateral spreading associated with an increase in channel width may have encouraged the deposition of a higher proportion of pebbles by decreasing the downstream flow momentum, as reflected by the fact that unconfined debris flows typically deposit on higher slope angles, and the lateral dissipation of excess pore pressures (Hungr et al., 1984; Benda and Cundy, 1990; Fannin and Wise, 2001; Guthrie et al., 2010). It is unclear why the frequency of

boulders decreases but the pebble content increases when the channel widens, to fully understand this relationship further observations must be made. Field observations from the 2018 catastrophic Montecito debris flows showed that the greatest rates of sediment recruitment and scour were in the fifth to seventh order channels, despite channel widening and decreasing gradient (Morell et al., 2021). Therefore, increases in channel width may not decrease the ability of catastrophic debris flows to transport boulders.

The Liusha debris flow fined downstream providing evidence for debulking (Makris et al., 2020), the recirculation of the coarsest grains (Johnson et al., 2012), or abrasion within the debris flow (Vallance and Scott, 1997) (Figure 9). Debulking is the deposition of coarse grains as the velocity decreases and the flow loses the ability to transport the coarsest grains (Makris et al., 2020). Consistent decreases in slope and increases in width downstream may mean this effect dominates in the smaller Liusha debris flow as the flow loses momentum and the ability to transport the largest grains. Alternatively, the recirculation and advection of coarse grains to levees once overtopped by the debris flow snout observed in flume experiments can also lead to the progressive loss of coarse grains in the distal sections of the flow (Johnson et al., 2012). This is unlikely to be the case here based on the absence of levees in both flows. Debris flow deposit GSDs have shown a tendency to become coarser or finer depending on the geology of the reach, which can alter the supply of particular grain sizes (Vallance and Scott, 1997; Berti et al., 1999; Tiranti et al., 2008). The shift from granitoids to greywacke shale and sandstones at approximately 900 m downstream in Liusha may lead to a change in the GSDs deposited by the debris flow. There is a distinctive fining of the flow near this change in geology, however a change in source or provenance was not obvious from field observations (Figures 2 and 9). The comparable geology from the source location in both catchments demonstrates that the GSD at the source may act as a stronger control on

469 downstream GSDs as opposed to a change in geology or through erosion and winnowing
470 within the flow.
471 No clear relationship was observed between the full GSDs deposited in Liusha and changes
472 in topography. For example, only a slight increase in the proportion of silt, clay and fine sand
473 deposited was observed with an increase in curvature, the opposite to our observation for the
474 Luoquan debris flow (Figures 9 and 10). Topography appears less important in governing the
475 deposition of different grain-size fractions in Liusha in comparison to Luoquan. The lack of
476 relationship may relate to the fact that changes in channel width in Liusha are more
477 systematic than in Luoquan and the channel is more constrained. The Liusha channel is also
478 steeper (minimum slope of 17° at most downstream position sampled) than Luoquan. The
479 fact that the Liusha debris flow travels a shorter distance (~1.5 km) before reaching the
480 tributary junction, and subsequently a sharp decrease in slope, could explain the differences
481 in runout length observed, considering the GSD is consistent for both flows.
482 From extensive analysis of two post-earthquake debris flow GSDs, we infer that the GSDs of
483 the two debris flows in Wenchuan do not explain the major differences observed in debris
484 flow runout length. In fact, both debris flows had statistically similar GSDs, which we
485 attributed to the similar source compositions with both flows triggered in Mesoproterozoic
486 granitoids and from co-seismic landslide deposits. The differences in runout length likely to
487 relate the high mobility of the large, catastrophic Luoquan debris flow, which is supported by
488 the lack of segregation within the deposit. We therefore reject the hypothesis that GSDs
489 control the runout length of debris flows in this instance, where both debris flows are
490 triggered from similar source material under similar conditions. The relationship between
491 grain size and topography was inconsistent, particularly with respect to slope and curvature,
492 for the full length of both debris flows. Differences in topography were also unlikely to
493 explain the large variation in debris flow runout, with the catastrophic Luoquan debris flow

494 able to sustain momentum, and reach extremely large volumes, even on a shallower slope.
495 Instead, sediment availability and higher water content are more likely to explain the
496 catastrophic 2019 Luoquan debris flow. Our conclusions are limited by sample size; however,
497 these results present some of the highest resolution GSDs to date for large debris flows and
498 only further methodological advances will enable more detailed measurements. Similarly, by
499 only measuring boulders where high-quality aerial imagery was available (1750 m), we were
500 unable to fully explore the relationship between boulder size and channel width. It would be
501 interesting to explore this relationship further for catastrophic debris flows to better constrain
502 the hazards posed by these flows, notably areas where entrainment and deposition are
503 greatest.
504 The GSDs presented here demonstrate the importance of source material and in-channel
505 sediment in controlling the GSD of debris flow deposits even in debris flows with different
506 runout lengths and dominant internal processes, such as grain size segregation. These
507 findings can be used when choosing more realistic representations, beyond the widely used
508 D_{50} values, to represent GSDs from natural debris flows in runout models. For example,
509 using the GSD integral could be more appropriate. Further field measurements should be
510 collected for debris flows with distinct differences between the source material and in
511 channel sediment. Analyzing the relative importance of both source material and in channel
512 sediment for debris flow runout length and GSDs will help to better account for each
513 sediment source in future debris flow hazard assessments (Morell et al., 2021). This work
514 further highlights the importance of considering in-channel sediment in debris flow runout
515 models. Current numerical modelling has demonstrated the role of sediment exchange
516 between flows and the bed in both dry granular flows (Edwards et al., 2021) and multiphase
517 flows (Ouyang et al., 2015; Horton et al., 2019). To understand the persistent hazard posed by
518 extremely large debris flows following the earthquake, further investigation into alternative

519 controls on runout length for catastrophic debris flows, such as sediment availability and
520 water content, is crucial.

521 **CONCLUSIONS**

522 We have presented some of the highest resolution GSDs collected for modern-day debris
523 flow deposits. The two debris flows studied had very different runout lengths, despite
524 occurring under similar initiation conditions and in close proximity. We hypothesized that
525 both debris flows deposited different GSDs with large variations in the fine sediment fraction
526 to explain the large differences in runout length. However, we found that both debris flows
527 deposited GSDs of a similar range and maximum grain size. The similar GSDs, particularly
528 with respect to the proportion of gravel, cobbles, and boulders, demonstrate that the different
529 runout lengths could not be explained by the deposit GSDs alone and therefore we accept the
530 null hypothesis. Both flows also deposited very minor fractions of clay and silt (<2% total
531 weight), which was on the lower boundary of previous field observations and highlights how
532 coarse these two deposits were. We believe the GSDs deposited were similar due to the fact
533 they were both triggered in similar geologies from co-seismic material. Our findings indicate
534 that the runout length of coarse-grained debris flows is not primarily related to the GSD
535 deposited. The spatial pattern of grain size throughout both flows differed. The most notable
536 difference was the presence of inverse grading in the middle sections of the smaller Liusha
537 debris flow in comparison to the lack of systematic segregation by grain size in the Luoquan
538 deposit. The absence of inverse grading in the larger deposit is thought to be driven by the
539 more fluidized-nature, and subsequently higher water content, associated with the larger
540 catastrophic debris flow, which can buffer grain contacts, and reduce the potential for
541 segregation within the flow. The GSDs deposited were also somewhat influenced by the
542 topography within the catchment, with channel width and curvature changing the proportion
543 of the grain-size fractions deposited in different reaches of the flow. The differences in the

spatial pattern of GSDs deposited in Liusha and Luoquan indicates that internal mechanisms can vary between debris flows with similar GSDs and different channel geometries.

ACKNOWLEDGMENTS

This work formed part of E.L Harvey's Ph.D. the- sis and was funded by grants awarded by the National Science Foundation Fund for Distinguished Young Scholars (42125702) and the Natural Environment Research Council (NE/L002434/1). Additional funding was also provided by the Tencent Foundation through the XPLORER PRIZE (XPLORER-2022-1012) and the Natural Science Foundation of Sichuan Province (2022NSFSC0003). We are grateful to Mikael Attal and Claire Earlie who provided comments on an earlier version of the manuscript and Pasquale Marino for assistance in the field. We are grateful to the associate editor and two anonymous reviewers, whose comments significantly improved this manuscript. The sieved GSDs and photos taken of the deposit surface can be accessed at https://doi.org/10.5281/zenodo .8074837 and cited as Harvey et al. (2023).

REFERENCES CITED

Attal, M., and Lavé, J., 2006, Changes of bedload characteristics along the Marsyandi River (central Nepal): Implications for understanding hillslope sediment supply, sediment load evolution along fluvial networks, and denudation in active orogenic belts: Tectonics, Climate, and Landscape Evolution, v. 398, p. 143–171, doi:10.1130/2006.2398(09).

Attal, M., Mudd, S.M., Hurst, M.D., Weinman, B., Yoo, K., and Naylor, M., 2015, Impact of change in erosion rate and landscape steepness on hillslope and fluvial sediments grain size in the Feather River basin (Sierra Nevada, California): Earth Surface Dynamics, v. 3, p. 201–222, doi:10.5194/esurf-3-201-2015.

Bagnold, R.A., 1954, Experiments on a gravity-free dispersion of large solid spheres in a Newtonian fluid under shear: Proceedings of the Royal Society of London. Series A. Mathematical and Physical Sciences, v. 225, p. 49–63, doi:10.1098/rspa.1954.0186.

569 Barker, T., Rauter, M., Maguire, E.S.F., Johnson, C.G., and Gray, J.M.N.T., 2021, Coupling
570 rheology and segregation in granular flows: Journal of Fluid Mechanics, v. 909,
571 doi:10.1017/jfm.2020.973.
572 Benda, L., 1990, The influence of debris flows on channels and valley floors in the Oregon
573 Coast Range, U.S.A: Earth Surface Processes and Landforms, v. 15, p. 457–466.
574 Benda, L., and Cundy, T.W., 1990, Predicting deposition of debris flows in mountain
575 channels: Canadian Geotechnical Journal, v. 27, p. 409–417.
576 Berti, M., Genevois, R., Simoni, A., and Tecca, P.R., 1999, Field observations of a debris
577 flow event in the Dolomites: Geomorphology, v. 29, p. 265–274, doi:10.1016/S0169-
578 555X(99)00018-5.
579 Blair, T.C., and McPherson, J.G., 1998, Recent debris-flow processes and resultant form and
580 facies of the dolomite alluvial fan, Owens Valley, California: Journal of Sedimentary
581 Research, v. 68, p. 800–818, doi:10.2110/jsr.68.800.
582 Bunte, K., and Abt, S.R., 2001, Sampling frame for improving pebble count accuracy in
583 coarse gravel-bed streams: Journal of the American Water Resources Association, v. 37,
584 p. 1001–1014, doi:10.1111/j.1752-1688.2001.tb05528.x.
585 Buscombe, D., 2013, Transferable wavelet method for grain-size distribution from images of
586 sediment surfaces and thin sections, and other natural granular patterns: Sedimentology,
587 v. 60, p. 1709–1732, doi:10.1111/sed.12049.
588 Cannon, S.H., Bigio, E.R., and Mine, E., 2001, A process for fire-related debris flow
589 initiation, Cerro Grande fire, New Mexico: Hydrological Processes, v. 15, p. 3011–3023,
590 doi:10.1002/hyp.388.
591 Cannon, S.H., and Savage, W.Z., 1988, A mass-change model for the estimation of debris
592 flow runout: Journal of Geology, v. 96, p. 221–227, doi:10.5962/bhl.part.18644.
593 Cenderelli, D.A., and Kite, J.S., 1998, Geomorphic effects of large debris flows on channel

morphology at North Fork Mountain, Eastern West Virginia, USA: Earth Surface Processes and Landforms, v. 23, p. 1–19.

Chen, H., Su, D., and Chen, K., 2001, Some Case Studies on the Engineering Geological Characteristics of Debris Flows in Taiwan: Western Pacific Earth Sciences, v. 1, p. 265–296.

Church, M.A., McLean, D.G., and Wolcott, J.F., 1987, River bed gravels: sampling and analysis, *in* Thorne, C.R., Bathurst, J.C., and Hey, R.D. eds., Gravel Bed Rivers, Chichester, John Wiley, p. 43–87.

Cleveland, W.S., 1979, Robust locally weighted regression and smoothing scatterplots: Journal of the American statistical association, v. 74, p. 829–836.

Domènech, G., Fan, X., Scaringi, G., van Asch, T.W.J., Xu, Q., Huang, R., and Hales, T.C., 2019, Modelling the role of material depletion, grain coarsening and revegetation in debris flow occurrences after the 2008 Wenchuan earthquake: Engineering Geology, v. 250, p. 34–44, doi:10.1016/j.enggeo.2019.01.010.

Dufresne, A., and Dunning, S.A., 2017, Process dependence of grain size distributions in rock avalanche deposits: Landslides, v. 14, p. 1555–1563, doi:10.1007/s10346-017-0806-y.

Dunning, S.A., 2006, The grain-size distribution of rock avalanche deposits in valley-confined settings: Italian Journal of Engineering Geology and Environment, v. 1, p. 117–121, doi:10.4408/IJEGE.2006-01.S-15.

Edwards, A.N., Viroulet, S., Johnson, C.G., and Gray, J.M.N.T., 2021, Erosion-deposition dynamics and long distance propagation of granular avalanches: Journal of Fluid Mechanics, v. 915, p. 1–40, doi:10.1017/jfm.2021.34.

Fannin, R.J., and Wise, M.P., 2001, An empirical-statistical model for debris flow travel distance: Canadian Geotechnical Journal, v. 38, p. 982–994, doi:10.1139/cgj-38-5-982.

619 Francis, O.R., Fan, X., Hales, T., Hobley, D., Xu, Q., and Huang, R., 2022, The Fate of
620 Sediment After a Large Earthquake: Journal of Geophysical Research: Earth Surface, v.
621 127, p. 1–19, doi:10.1029/2021jf006352.
622 Genevois, R., Tecca, P.R., Berti, M., and Simoni, A., 2000, Debris flows in Dolomites :
623 experimental data from a monitoring system: 2nd International Conference on Debris-
624 Flow Hazard Mitigation,.
625 Gray, J.M.N.T., Gajjar, P., and Kokelaar, P., 2015, Particle-size segregation in dense granular
626 avalanches: Comptes Rendus Physique, v. 16, p. 73–85, doi:10.1016/j.crhy.2015.01.004.
627 Guo, X., Cui, P., Li, Y., Zou, Q., and Kong, Y., 2016, The formation and development of
628 debris flows in large watersheds after the 2008 Wenchuan Earthquake: Landslides, v.
629 13, p. 25–37, doi:10.1007/s10346-014-0541-6.
630 Guthrie, R.H., Hockin, A., Colquhoun, L., Nagy, T., Evans, S.G., and Ayles, C., 2010, An
631 examination of controls on debris flow mobility: Evidence from coastal British
632 Columbia: Geomorphology, v. 114, p. 601–613, doi:10.1016/j.geomorph.2009.09.021.
633 de Haas, T., Braat, L., Leuven, J.R.F.W., Lokhorst, I.R., and Kleinhans, M.G., 2015, Effects
634 of debris flow composition on runout, depositional mechanisms, and deposit
635 morphology in laboratory experiments: Journal of Geophysical Research: Earth Surface,
636 v. 120, p. 1949–1972, doi:10.1002/2015JF003525.
637 Harvey, E.L., Hales, T.C., Hobley, D.E.J., Liu, J., and Fan, X., 2022, Measuring the grain-
638 size distributions of mass movement deposits: Earth Surface Processes and Landforms,
639 p. 1–16, doi:10.1002/esp.5337.
640 Harvey, E.L., Hales, T.C., Liu, J., Hobley, D.E.J., Fan, Y., Xia, B., and Fan, X., 2023, Grain
641 size variability in debris flows of different runout lengths, Wenchuan, China: Zenodo,
642 https://doi.org/10.5281/zenodo.8074837.
643 Horton, A.J., Hales, T.C., Ouyang, C., and Fan, X., 2019, Identifying post-earthquake debris

644 flow hazard using Massflow: Engineering Geology, v. 258,
645 doi:10.1016/j.enggeo.2019.05.011.
646 Hungr, O., McDougall, S., Wise, M., and Cullen, M., 2008, Magnitude-frequency
647 relationships of debris flows and debris avalanches in relation to slope relief:
648 Geomorphology, v. 96, p. 355–365, doi:10.1016/j.geomorph.2007.03.020.
649 Hungr, O., Morgan, G.C., and Kellerhals, R., 1984, Quantitative analysis of debris torrent
650 hazards for design of remedial measures.: Canadian Geotechnical Journal, v. 21, p. 663–
651 677, doi:10.1139/t84-073.
652 Iverson, R.M., 1997, The Physics of Debris Flows: Review of Geophysics, v. 35, p. 245–296.
653 Iverson, R.M., Logan, M., LaHusen, R.G., and Berti, M., 2010, The perfect debris flow?
654 Aggregated results from 28 large-scale experiments: Journal of Geophysical Research,
655 v. 115, doi:10.1029/2009jf001514.
656 Iverson, R.M., Reid, M.E., Logan, M., LaHusen, R.G., Godt, J.W., and Griswold, J.P., 2011,
657 Positive feedback and momentum growth during debris-flow entrainment of wet bed
658 sediment: Nature Geoscience, v. 4, p. 116–121, doi:10.1038/ngeo1040.
659 Johnson, C.G., Kokelaar, B.P., Iverson, R.M., Logan, M., Lahusen, R.G., and Gray,
660 J.M.N.T., 2012, Grain-size segregation and levee formation in geophysical mass flows:
661 Journal of Geophysical Research: Earth Surface, v. 117, p. 1–23,
662 doi:10.1029/2011JF002185.
663 Johnson, A.M., and Rodine, J.R., 1984, Debris Flow, *in* Slope Instability, p. 257–361,
664 doi:10.1201/noe0849338304.ch78.
665 Jones, R.P., Rengers, F.K., Barnhart, K.R., George, D.L., Staley, D.M., and Kean, J.W.,
666 2023, Simulating debris flow and levee formation in the 2D shallow flow model D-
667 Claw: Channelized and unconfined flow: Earth and Space Science, v. 10, p. 1–20,
668 doi:10.1029/2022ea002590.

669 Kaitna, R., Palucis, M.C., Yohannes, B., Hill, K.M., and Dietrich, W.E., 2016, Effects of
670 coarse grain size distribution and fine particle content on pore fluid pressure and shear
671 behavior in experimental debris flows: Journal of Geophysical Research: Earth Surface,
672 v. 121, p. 415–441, doi:10.1002/2015JF003725.
673 Kellerhals, R., and Bray, D., 1971, Sampling Procedures for Coarse Fluvial Sediments:
674 Journal of the Hydraulics Division, v. 97, p. 1165–1180.
675 Kim, S.B., Chough, S.K., and Chun, S.S., 1995, Bouldery deposits in the lowermost part of
676 the Cretaceous Kyokpori Formation, SW Korea: cohesionless debris flows and debris
677 falls on a steep-gradient delta slope: Sedimentary Geology, v. 98, p. 97–119,
678 doi:10.1016/0037-0738(95)00029-8.
679 Kim, B.C., and Lowe, D.R., 2004, Depositional processes of the gravelly debris flow
680 deposits, South Dolomite alluvial fan, Owens Valley, California: Geosciences Journal,
681 v. 8, p. 153–170.
682 Lanzoni, S., Gregoretti, C., and Stancanelli, L.M., 2017, Coarse-grained debris flow
683 dynamics on erodible beds: Journal of Geophysical Research: Earth Surface, v. 122, p.
684 592–614, doi:10.1002/2016JF004046.
685 Ma, L., 2002, Geological Atlas of China: Beijing, Geological Publishing House.
686 Major, J.J., 1997, Depositional processes in large-scale debris-flow experiments: Journal of
687 Geology, v. 105, p. 345–366, doi:10.1086/515930.
688 Major, J.J., and Iverson, R.M., 1999, Debris-flow deposition: Effects of pore-fluid pressure
689 and friction concentrated at flow margins: GSA Bulletin, v. 111, p. 1424–1434.
690 Major, J.J., and Pierson, T.C., 1992, Debris Flow Rheology' Experimental Analysis of Fine-
691 Grained Slurries:
692 Major, J.J., Pierson, T.C., and Scott, K.M., 2007, Debris flows at Mount St. Helens,
693 Washington, USA: Debris-flow Hazards and Related Phenomena, p. 685–731,

694 doi:10.1007/3-540-27129-5_27.
695 Makris, S., Manzella, I., Cole, P., and Roverato, M., 2020, Grain size distribution and
696 sedimentology in volcanic mass-wasting flows: implications for propagation and
697 mobility: International Journal of Earth Sciences, doi:10.1007/s00531-020-01907-8.
698 Morell, K.D., Alessio, P., Dunne, T., and Keller, E., 2021, Sediment Recruitment and
699 Redistribution in Mountain Channel Networks by Post-Wildfire Debris Flows:
700 Geophysical Research Letters, v. 48, p. 1–10, doi:10.1029/2021GL095549.
701 Ouyang, C., He, S., and Tang, C., 2015, Numerical analysis of dynamics of debris flow over
702 erodible beds in Wenchuan earthquake-induced area: Engineering Geology, v. 194, p.
703 62–72, doi:10.1016/j.enggeo.2014.07.012.
704 Pierson, T.C., 1981, Dominant particle support mechanisms in debris flows at Mt Thomas,
705 New Zealand, and implications for flow mobility: Sedimentology, v. 28, p. 49–60,
706 doi:10.1111/j.1365-3091.1981.tb01662.x.
707 Pierson, T.C., and Costa, J.E., 1987, A rheologic classification of subaerial sediment-water
708 flows: GSA Reviews in Engineering Geology, v. 7, p. 1–12, doi:10.1130/REG7-p1.
709 Prochaska, A.B., Santi, P.M., Higgins, J.D., and Cannon, S.H., 2008, A study of methods to
710 estimate debris flow velocity: Landslides, v. 5, p. 431–444, doi:10.1007/s10346-008-
711 0137-0.
712 Purinton, B., and Bookhagen, B., 2021, Tracking Downstream Variability in Large Grain-
713 Size Distributions in the South-Central Andes: Journal of Geophysical Research: Earth
714 Surface, v. 126, p. 1–29, doi:10.1029/2021jf006260.
715 Santi, P.M., deWolfe, V.G., Higgins, J.D., Cannon, S.H., and Gartner, J.E., 2008, Sources of
716 debris flow material in burned areas: Geomorphology, v. 96, p. 310–321,
717 doi:10.1016/j.geomorph.2007.02.022.
718 Sanvitale, N., and Bowman, E.T., 2017, Visualization of dominant stress-transfer

719 mechanisms in experimental debris flows of different particle-size distribution:
720 Canadian Geotechnical Journal, v. 54, p. 258–269, doi:10.1139/cgj-2015-0532.
721 Scheidl, C., McArdell, B.W., and Rickenmann, D., 2015, Debris-flow velocities and
722 superelevation in a curved laboratory channel: Canadian Geotechnical Journal, v. 52, p.
723 305–317, doi:10.1139/cgj-2014-0081.
724 Shakesby, R.A., and Matthews, J.A., 2002, Sieve deposition by debris flow on a permeable
725 substrate, Leirdalen, Norway: Earth Surface Processes and Landforms, v. 27, p. 1031–
726 1041, doi:10.1002/esp.390.
727 Shultz, A.W., 1984, Subaerial debris-flow deposition in the upper paleozoic cutler formation,
728 western Colorado: Journal of sedimentary petrology, v. 54, p. 759–772.
729 Sklar, L.S., Riebe, C.S., Genetti, J., Leclere, S., and Lukens, C.E., 2020, Downvalley fining
730 of hillslope sediment in an alpine catchment: implications for downstream fining of
731 sediment flux in mountain rivers: Earth Surface Processes and Landforms, v. 45, p.
732 1828–1845, doi:10.1002/esp.4849.
733 Sklar, L.S., Riebe, C.S., Marshall, J.A., Genetti, J., Leclere, S., Lukens, C.L., and Merces, V.,
734 2017, The problem of predicting the size distribution of sediment supplied by hillslopes
735 to rivers: Geomorphology, v. 277, p. 31–49, doi:10.1016/j.geomorph.2016.05.005.
736 Sohn, Y.K., Rhee, C.W., and Kim, B.C., 1999, Debris flow and hyperconcentrated flood-flow
737 deposits in an alluvial fan, northwestern part of the Cretaceous Yongdong Basin, Central
738 Korea: Journal of Geology, v. 107, p. 111–132, doi:10.1086/314334.
739 Sosio, R., Crosta, G.B., and Frattini, P., 2007, Field observations, rheological testing and
740 numerical modelling of a debris-flow event: Earth Surf. Process. Landforms, v. 32, p.
741 290–306, doi:10.1002/esp.
742 Takahashi, T., 2007, Debris flow: mechanics, prediction and countermeasures.: Taylor &
743 Francis.

744 Takahashi, T., 1981, Debris Flow: Annu. Rev. Fluid Mech, v. 13, p. 57–77.
745 Takahashi, B.T., Nakagawa, H., Harada, T., and Yamashiki, Y., 1992, Routing debris flows
746 with particle segregation: Journal of Hydraulic Engineering, v. 118, p. 1490–1507.
747 Tang, C., Van Asch, T.W.J., Chang, M., Chen, G.Q., Zhao, X.H., and Huang, X.C., 2012,
748 Catastrophic debris flows on 13 August 2010 in the Qingping area, southwestern China:
749 The combined effects of a strong earthquake and subsequent rainstorms:
750 Geomorphology, v. 139–140, p. 559–576, doi:10.1016/j.geomorph.2011.12.021.
751 Tiranti, D., Bonetto, S., and Mandrone, G., 2008, Quantitative basin characterisation to refine
752 debris-flow triggering criteria and processes: An example from the Italian Western Alps:
753 Landslides, v. 5, p. 45–57, doi:10.1007/s10346-007-0101-4.
754 Vallance, J.W., and Savage, S.B., 2000, Particle segregation in granular flows down chutes,
755 *in* Rosato, A. and Blackmore, D. eds., International Union of Theoretical and Applied
756 Mechanics Symposium on Segregation in Granular Flows, Dordrecht, The Netherlands,
757 p. 31–51.
758 Vallance, J.W., and Scott, K.M., 1997, The Osceola Mudflow from Mount Rainier:
759 Sedimentology and hazard implications of a huge clay-rich debris flow: Bulletin of the
760 Geological Society of America, v. 109, p. 143–163.
761 Whipple, K.X., and Dunne, T., 1992, The influence of debris-flow rheology on fan
762 morphology, Owens Valley, California: Geological Society Of America Bulletin, v. 104,
763 p. 887–900.
764 Yang, F., Fan, X., Siva Subramanian, S., Dou, X., Xiong, J., Xia, B., Yu, Z., and Xu, Q.,
765 2021, Catastrophic debris flows triggered by the 20 August 2019 rainfall, a decade since
766 the Wenchuan earthquake, China: Landslides, v. 18, p. 3197–3212, doi:10.1007/s10346-
767 021-01713-6.
768

769

770 Table 1. Table displaying the characteristics of the Liusha and Luoquan debris-flow events

	Luoquan	**Liusha**
Event date	20th August 2019	20th August 2019
Rainfall on 19th and 20th August (mm)	184	175
Longitude	103.518	103.33
Latitude	31.199	31.119
Number of sampling locations	8	4
Debris Flow Area[*] (m^2)	420 000	33 000
Runout Length[*] (m)	8000	1500
Elevation change[†] (m)	950	750
Elevation change[§] (m)	470	324
Average slope[#] (°)	7	27
Average slope[**] (°)	9	23
Average width[**] (m)	42	8

[*] Area and runout includes source (approximate) and deposit.
[†] Elevation change for full debris flow from triggering location.
[§] Elevation change between the most upstream and most downstream pit location.
[#] Average slope based on the first derivative of elevation, measured from a 30 m JAXA DEM.
[**] Average slope and width based on field measurements

771

772

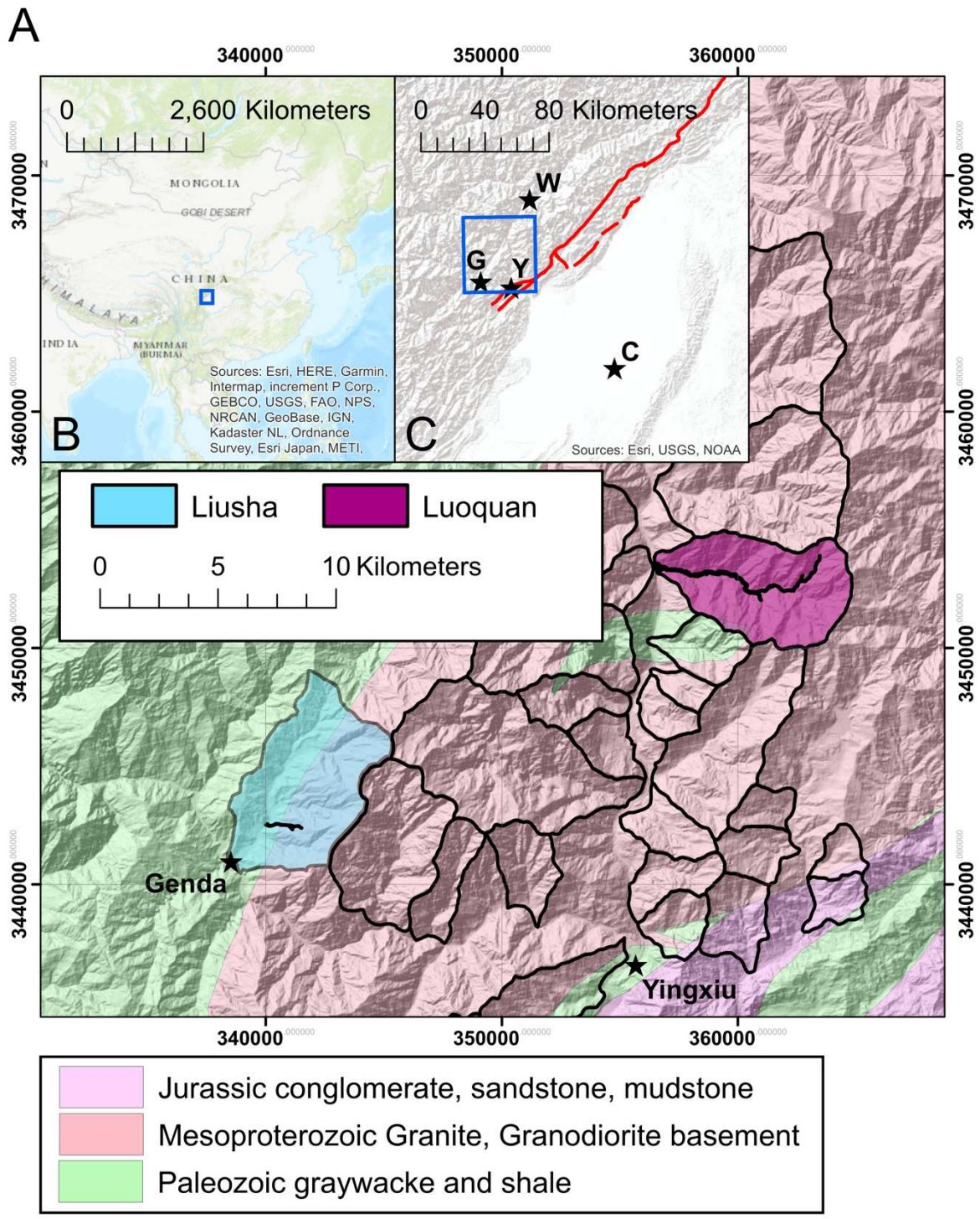

773

774 Figure 1. Map showing the Liusha and Luoquan debris flows in their respective catchments.

775 The location of the catchments in China and relative to the fault traces ruptured by the 2008

776 Wenchuan Earthquake (red) as well as local towns (G- Genda, W – Wenchuan and Y –

777 Yingxiu) and cities (C – Chengdu) are shown in inset maps 1B and 1C. The underlying

778 geology in the region is also mapped using data from (Ma, 2002).

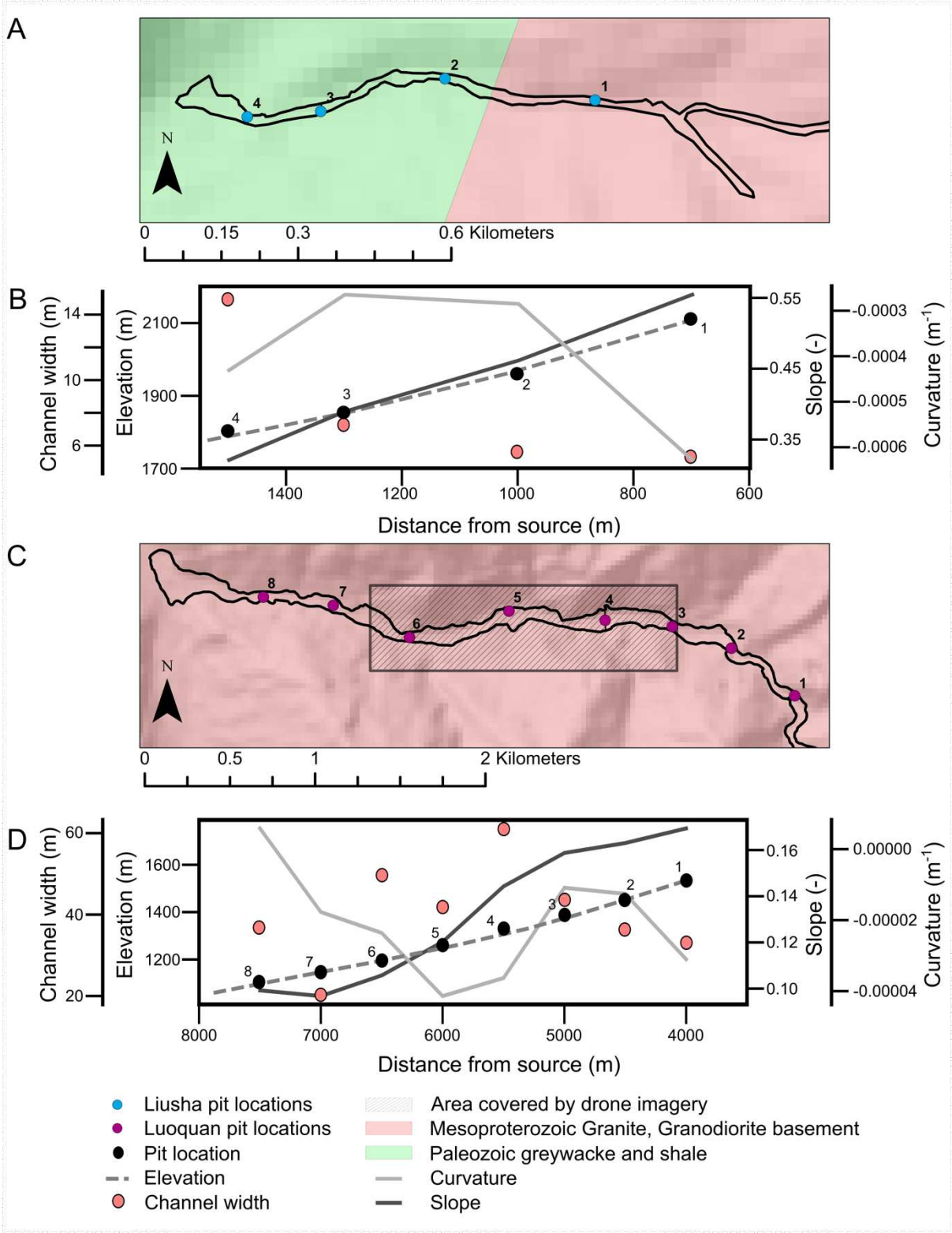

779

780 Figure 2. The location of the sieved pits, photo cross sections, and drone grain size

781 measurements for the Liusha (2A) and Luoquan (2C) debris flow deposits. The

geomorphological context for each deposit (elevation, slope, curvature and channel width) are shown in Figures 2B and 2D. The DEM used to produce the hillshade for both figures is 30 m resolution.

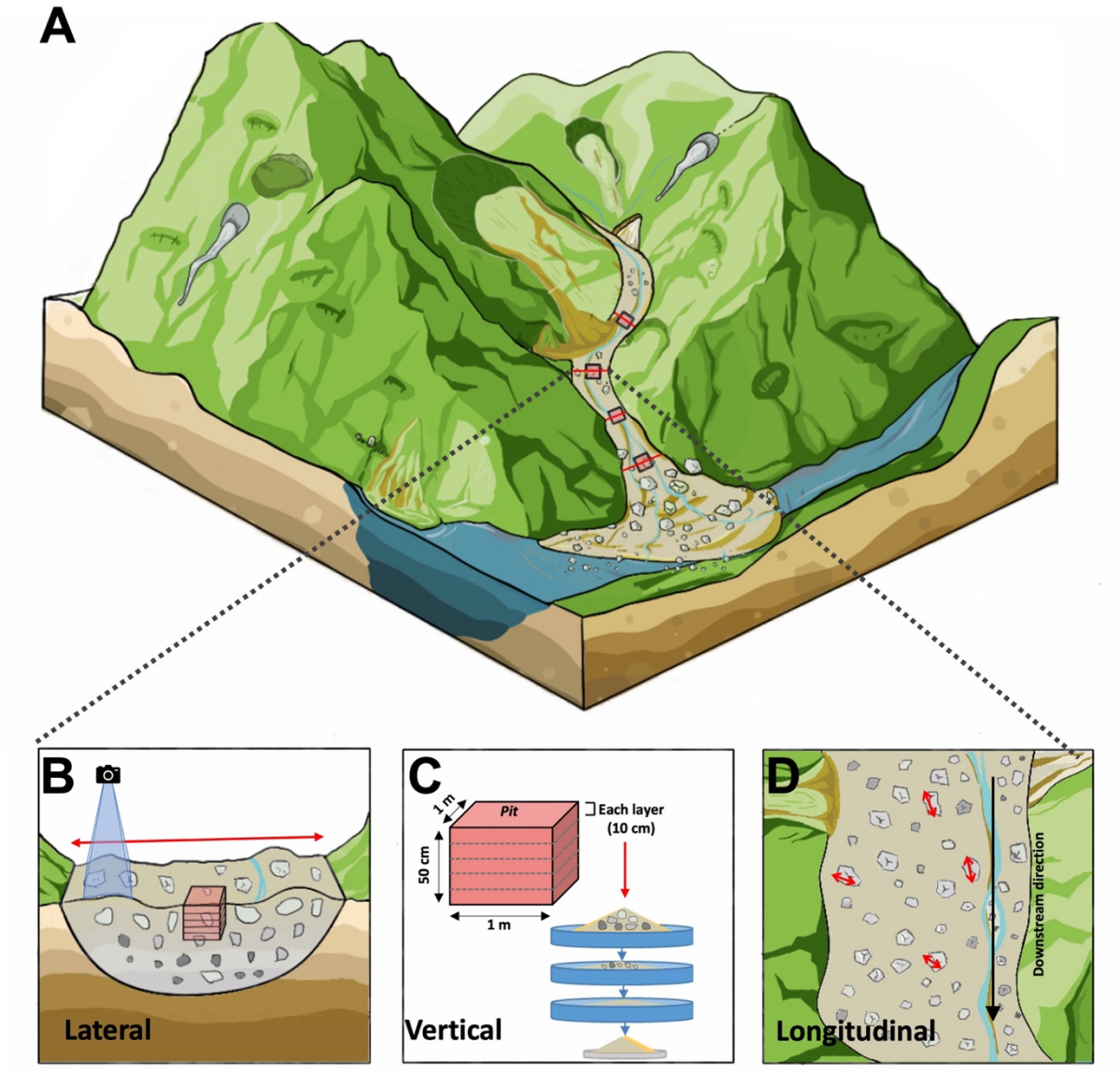

Figure 3. An overview of the methods used to measure the grain size of debris flow deposits. The insets show the approaches used to collect lateral grain size distributions from surface photos taken along channel cross sections (3B), vertical grain size distributions from sieved pits (3C) and longitudinal grain size distributions from surface photos and drone imagery (3D).

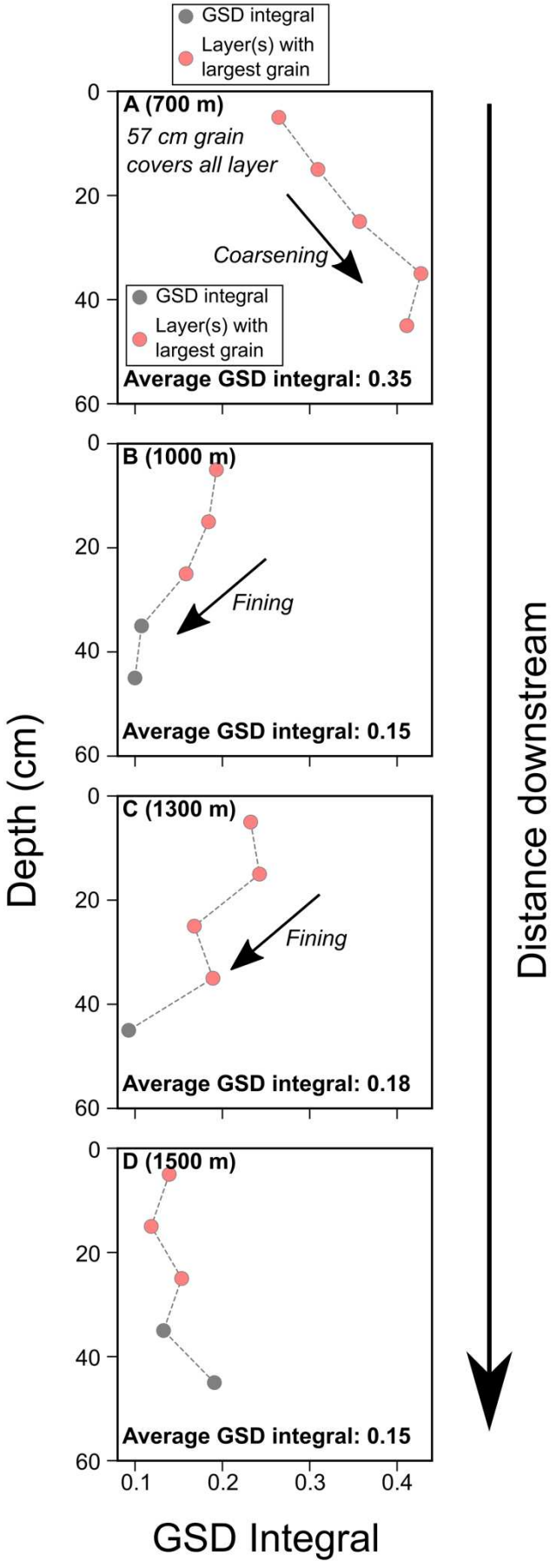
GSD integral
Layer(s) with largest grain
A (700 m)
57 cm grain covers all layer
Coarsening
GSD integral
Layer(s) with largest grain
Average GSD integral: 0.35
B (1000 m)
Fining
Average GSD integral: 0.15
C (1300 m)
Fining
Average GSD integral: 0.18
D (1500 m)
Average GSD integral: 0.15
Depth (cm)
0
20
40
60
0.1
0.2
0.3
0.4
GSD Integral
Distance downstream

792

793 Figure 4. The change in grain size distribution integral with depth for the Liusha debris flow.
794 Average grain size distribution integral is the average integral based on the grain size
795 distribution integrals calculated for each layer in the pit. Symbols in red show the layer(s)
796 which include the largest grain in each pit.

797

798

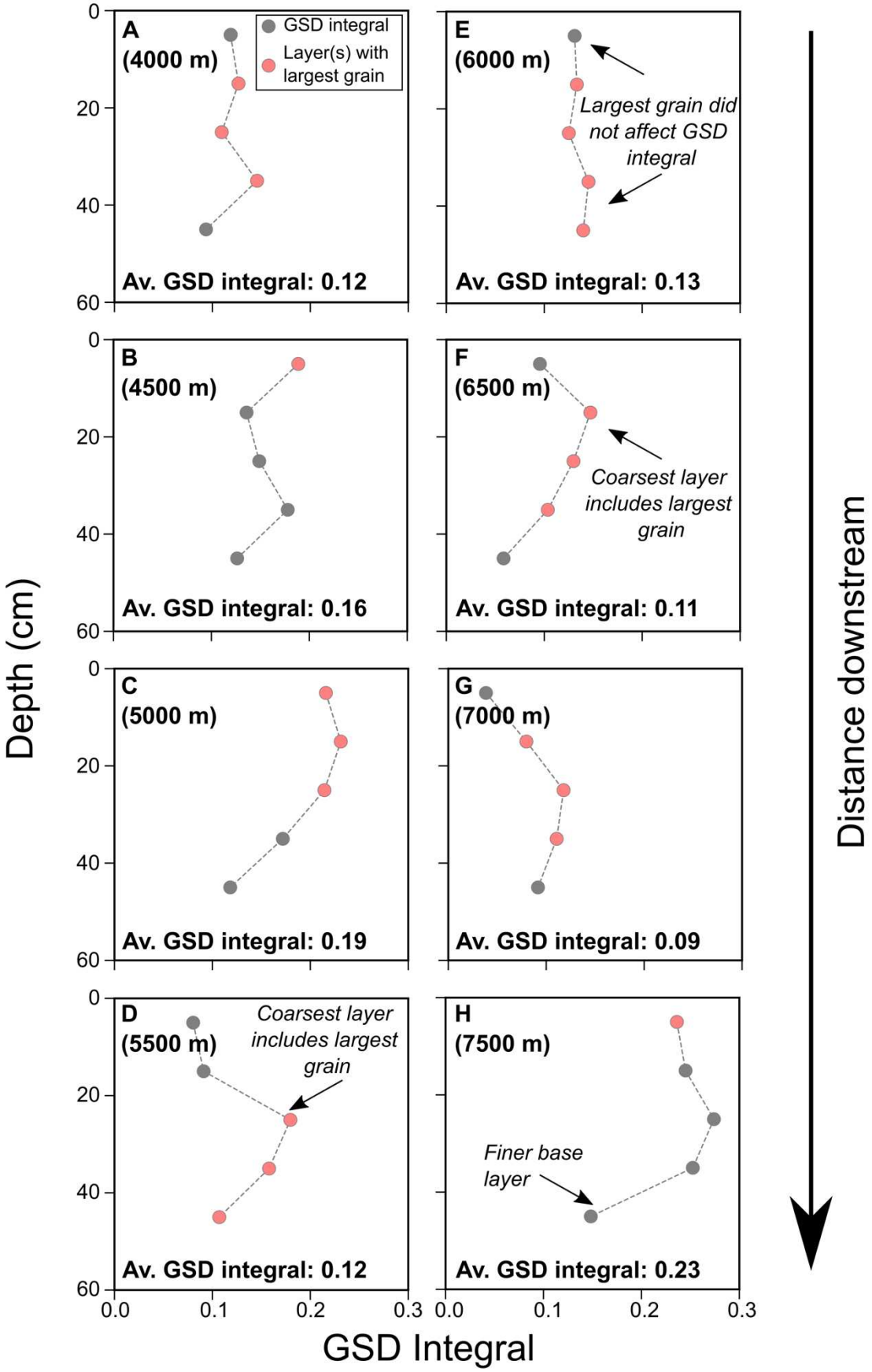
A
(4000 m)
GSD integral
Layer(s) with largest grain
Av. GSD integral: 0.12
E
(6000 m)
Largest grain did not affect GSD integral
Av. GSD integral: 0.13
B
(4500 m)
Av. GSD integral: 0.16
F
(6500 m)
Coarsest layer includes largest grain
Av. GSD integral: 0.11
C
(5000 m)
Av. GSD integral: 0.19
G
(7000 m)
Av. GSD integral: 0.09
D
(5500 m)
Coarsest layer includes largest grain
Av. GSD integral: 0.12
H
(7500 m)
Finer base layer
Av. GSD integral: 0.23
Depth (cm)
0
20
40
60
0.0
0.1
0.2
0.3
GSD Integral
Distance downstream

799

800 Figure 5. The change in grain size distribution integral with depth for the Luoquan debris
801 flow. Average grain size distribution integral is the average integral based on the grain size
802 distribution integrals calculated for each layer in the pit. Symbols in red show the layer(s)
803 which include the largest grain in each pit.
804
805

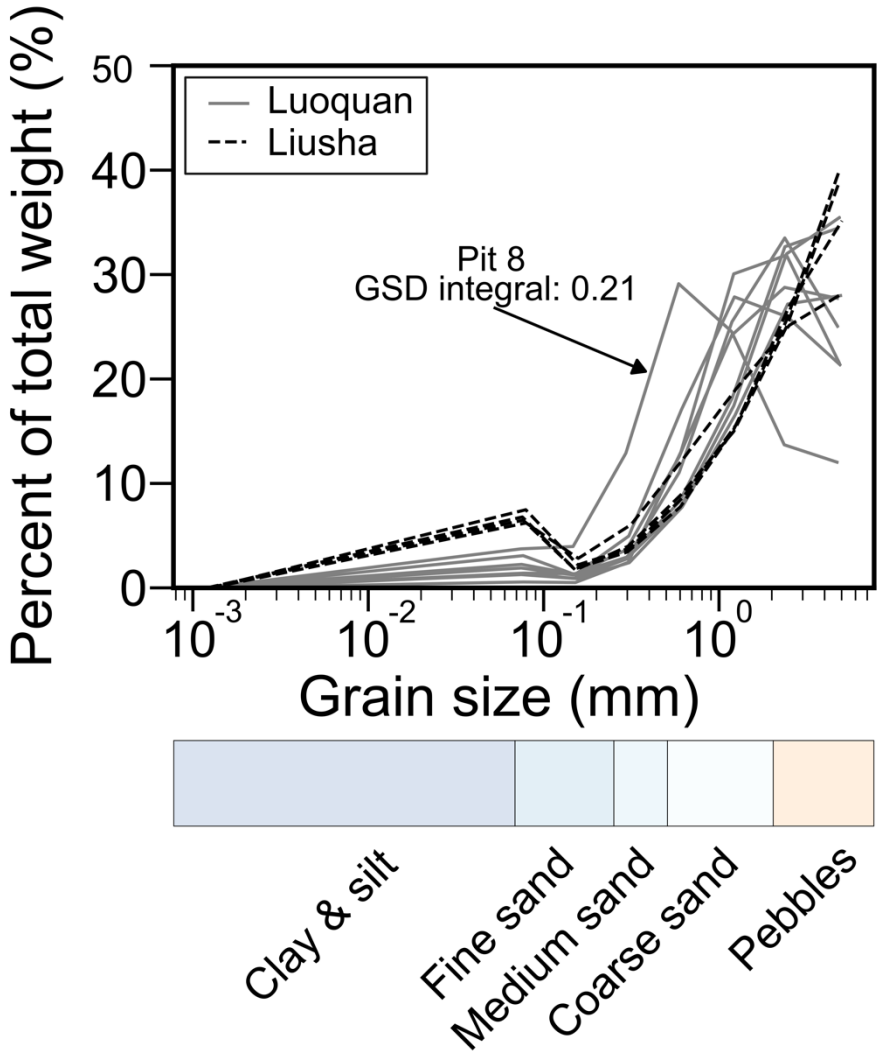

806
807 Figure 6. The proportion of grains by weight for each sieving size fraction relative to the total
808 proportion of grains <5 mm by weight for the Luoquan (solid grey line) and Liusha (dotted
809 black line) debris flows. These curves correspond to GSD integrals (plotted by percent
810 coarser than) in Table S2.

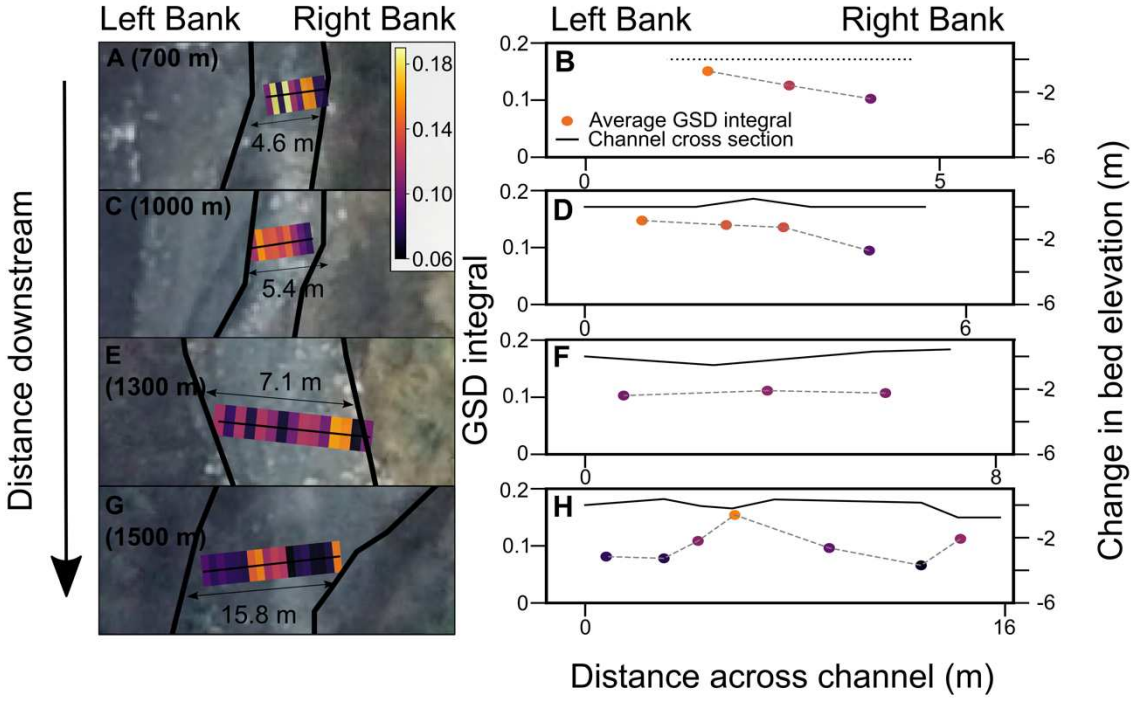

811

812 Figure 7. Plots showing lateral changes in the surface grain size distributions deposited for
813 the Liusha debris flow. The grain size distributions are based on surface photos which were
814 analyzed using pyDGS or manual photo counts. The grain size distribution for each photo is
815 represented by a colored bar which corresponds to the grain size distribution integral
816 (calculated using a D_{max} of 399 mm). The grain size distribution integral ranged from 0.06 to
817 0.19. A, C, E and G). The left and right banks of the deposit when facing downstream are
818 indicated. The black line shows the extent of the 2019 deposit. B, D, F and H) show the
819 cross-sectional area measured using a laser range finder and the average grain size
820 distribution integral for each geomorphic section. The average grain size distribution integral
821 is calculated by averaging the grain size distribution integrals for each geomorphic section,
822 which is defined by a change in slope. Note in Figure 7F by averaging across the geomorphic
823 section the coarse GSD in Figure 7E is hidden. The distance of the pit downstream is shown
824 in brackets next to the figure ID.

825

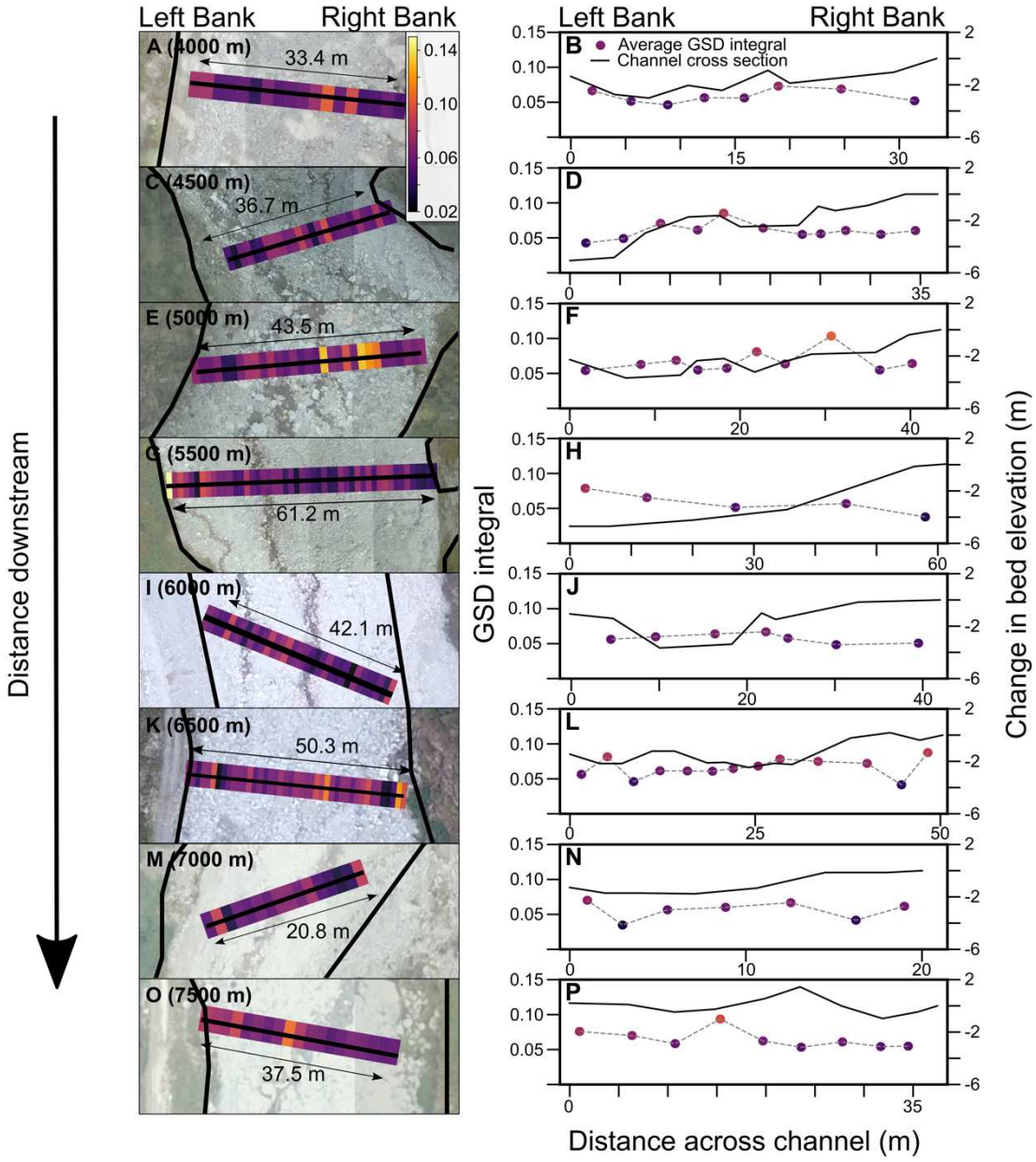

826

827 Figure 8. Plots showing lateral changes in the surface grain size distribution deposited for the
828 Luoquan debris flow. The grain size distributions are based on surface photos which were
829 analyzed using pyDGS or manual photo counts. The grain size distribution for each photo is
830 represented by a colored bar which corresponds to the grain size distribution integral
831 (calculated using a D_{max} of 801 mm). The grain size distribution integral ranged from 0.02 to
832 0.15. A, C, E, G, I, K, M and O). The left and right banks of the deposit when facing
833 downstream are indicated. The black line shows the extent of the 2019 deposit. B, D, F, H, J,

L, N and P show the cross-sectional area measured using a laser range finder and the average grain size distribution integral for each geomorphic section. The average grain size distribution integral is calculated by averaging the grain size distribution integrals for each geomorphic section, which is defined by a change in slope. The distance of the pit downstream is shown in brackets next to the figure ID.

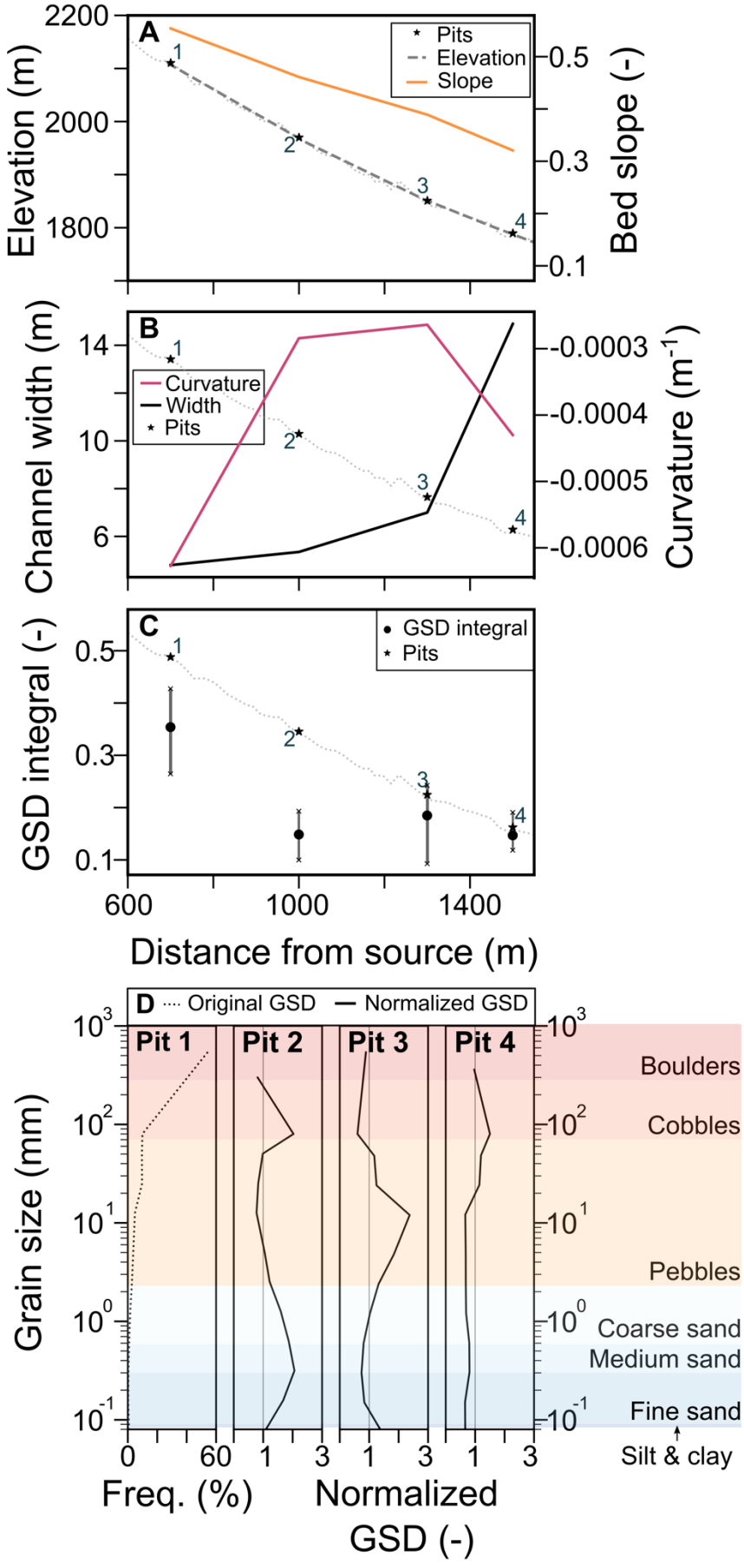
A
Pits
Elevation
Slope
Elevation (m)
Bed slope (-)
B
Curvature
Width
Pits
Channel width (m)
Curvature (m-1)
C
GSD integral
Pits
GSD integral (-)
Distance from source (m)
D
Original GSD
Normalized GSD
Pit 1
Pit 2
Pit 3
Pit 4
Grain size (mm)
Boulders
Cobbles
Pebbles
Coarse sand
Medium sand
Fine sand
Silt & clay
Freq. (%)
Normalized GSD (-)

840 Figure 9.

841 Change in surface and subsurface grain size distributions with distance downstream for the
842 Liusha debris flow based on sieved pits (Figure 3). A) shows the elevation and slope at each
843 pit. B) shows the curvature and channel width for each pit. C) shows the grain size
844 distribution integral calculated by averaging across each sieved pit, as shown in Figure 4. The
845 grey error bars show the maximum and minimum grain size distribution integral for each pit.
846 The high GSD integral at Pit 1 reflects the fact that the GSD integral best represents the
847 coarse fraction and that Pit 1 is particularly coarse. D) The grain size distribution shown for
848 Pit 1 is the original sieved grain size distribution for the full 50 cm profile as a probability
849 density function. The following three pits then show normalized grain size distributions based
850 on the grain size distribution immediately upstream. A value >1 indicates that there has been
851 an increase in that grain-size fraction being deposited and a value <1 indicates that there has
852 been a decrease in that size fraction.

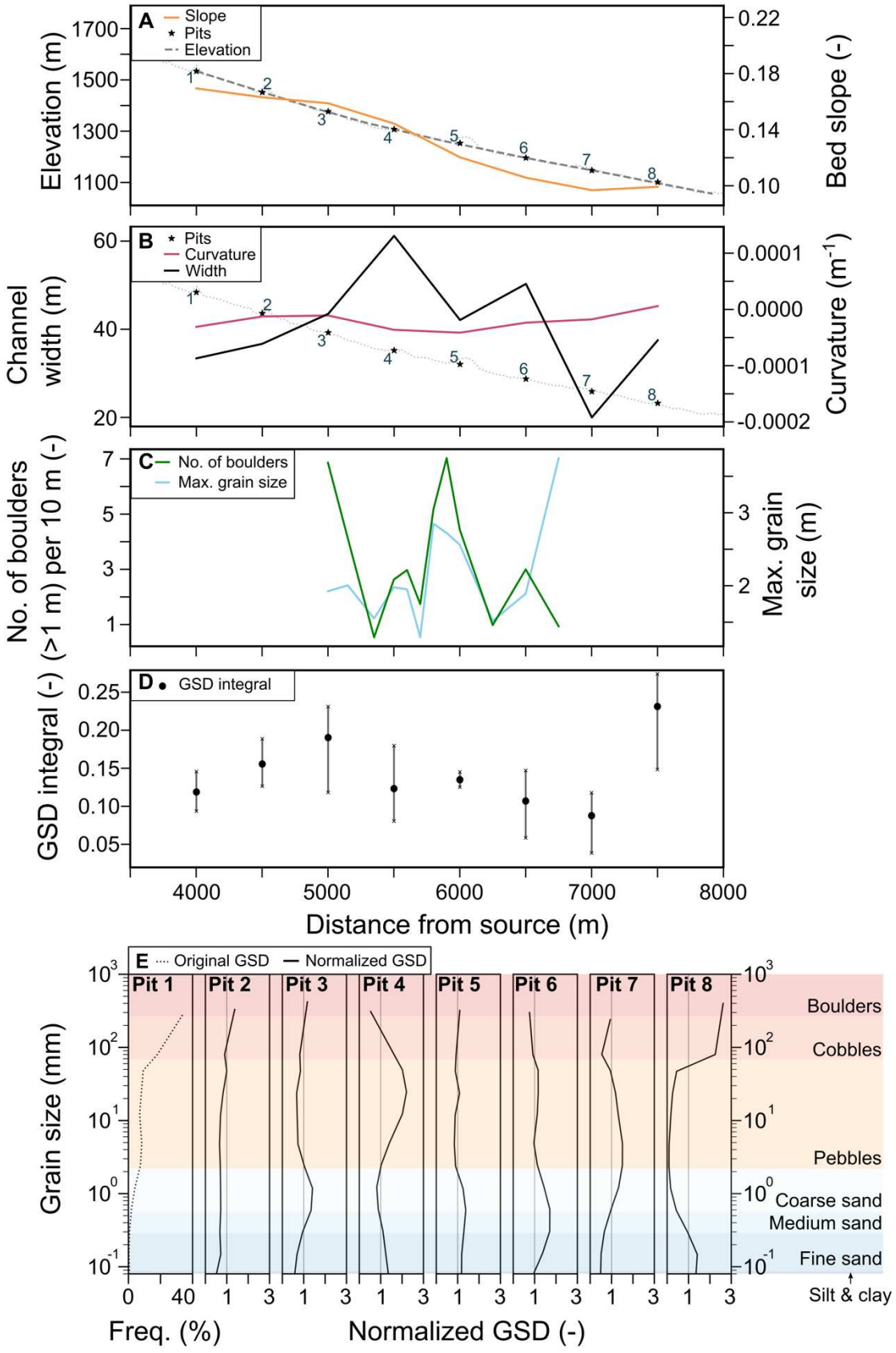
A
Slope
Pits
Elevation
Elevation (m)
Bed slope (-)
B
Pits
Curvature
Width
Channel width (m)
Curvature (m-1)
C
No. of boulders
Max. grain size
No. of boulders (>1 m) per 10 m (-)
Max. grain size (m)
D
GSD integral
GSD integral (-)
Distance from source (m)
E
Original GSD
Normalized GSD
Pit 1
Pit 2
Pit 3
Pit 4
Pit 5
Pit 6
Pit 7
Pit 8
Grain size (mm)
Boulders
Cobbles
Pebbles
Coarse sand
Medium sand
Fine sand
Silt & clay
Freq. (%)
Normalized GSD (-)

853

Figure 10. Comparisons between these figures display the relationship between topographic characteristics, drone grain size measurements and normalized grain size distributions for the Luoquan debris flow. The grain size distribution integrals and grain size distributions are based on surface and subsurface sieving profiles (Figure 3). A) shows the elevation and slope at each pit. B) shows the curvature and channel width for each pit. C) shows the maximum grain size and number of boulders greater than 1 m measured from drone imagery between 5000 and 6750 m downstream (see Figure 2C). D) shows the average grain size distribution integral calculated by averaging across each pit (see Figure 5) and the error bars with the maximum and minimum grain size distribution integral for each pit. E) shows the original sieved grain size distribution for Pit 1 (pit furthest upstream) across the full 50 cm profile as a probability density function, followed by normalized grain size distributions for Pits 2, 3, 4, 5, 6, 7 and 8 respectively. The normalized grain size distribution is calculated by dividing the grain size distribution of each pit by the grain size distribution of the previous pit. A value >1 indicates that there has been an increase in that grain-size fraction being deposited and a value <1 indicates that there has been a decrease in that size fraction.